Supplementary Information for

Emissive Charge-Transfer Excited-State at Well-Defined Hetero-Nanostructure Interface of Organic Conjugated Molecule and Two-Dimensional Inorganic Nanosheet

Tomokazu Umeyama,*[a] Daizu Mizutani,[b] Yuki Ikeda,[b] W. Ryan Osterloh,[b] Futa Yamamoto,[a] Kosaku Kato,[c] Akira Yamakata,*[c] Masahiro Higashi,*[b] Takumi Urakami,[b] Hirofumi Sato,[b] and Hiroshi Imahori*[bde]

[a.] Department of Applied Chemistry, Graduate School of Engineering, University of Hyogo, Himeji, Hyogo 671-2280, Japan
[b.] Department of Molecular Engineering, Graduate School of Engineering, Kyoto University, Kyoto 615-8510, Japan
[c.] Graduate School of Natural Science and Technology, Okayama University, Okayama 700-8530, Japan
[d.] Institute for Integrated Cell-Material Sciences (WPI-iCeMS), Kyoto University, Nishikyo-ku, Kyoto 615-8510, Japan
[e.] Institute for Liberal Arts and Sciences (ILAS), Kyoto University, Kyoto 606-8316, Japan

E-mail: umeyama@eng.u-hyogo.ac.jp, yamakata@okayama-u.ac.jp, higashi@moleng.kyoto-u.ac.jp, imahori@scl.kyoto-u.ac.jp

List of Contents

1. Instruments

Planetary ball-milling was performed on Fritsch Pulverisette 7 classic line by using a Si_3N_4 bowl (12 mL) with Si_3N_4 balls (5 mm diameter) under an argon atmosphere.

Atomic force microscopy (AFM) analyses were conducted with an Asylum Technology MFP-3D-SA in the AC mode. The dispersion in NMP was spin-coated on a freshly cleaved mica at 2000 rpm. Field emission scanning electron microscopy (FE-SEM) observation was carried out with a Hitachi SU8220. Energy Dispersive X-ray Spectroscopy (EDX) mappings were conducted with Horiba EMAXEvolution X-Max. Attenuated total reflectance (ATR) Fourier transform infrared (FT-IR) spectra were recorded on a Themo Fisher Scientific Nicolet 6700 FTIR. Resonant Raman spectra and mappings were recorded using a Horiba JobinYvon LabRAM ARAMIS equipped with excitation wavelengths of 2.33 eV (532 nm) and 1.96 eV (633 nm). X-ray photoelectron spectroscopy (XPS) was carried out with a ULVAC-PHI MT-5500 system with Mg K_α. Thermogravimetric analysis (TGA) measurements were conducted with a SHIMADZU DTG-60 under flowing nitrogen at a scan rate of 10 °C min^{-1}. ^1H NMR and ^{13}C NMR spectra were measured with a JEOL JNM-EX400 NMR spectrometer. High-resolution mass spectra were measured on a Thermo Fisher Scientific EXACTIVE (APCI).

UV−vis absorption spectra were measured with a Perkin-Elmer Lambda 900 UV/vis/NIR spectrometer or Shimadzu UV-3600i Plus. Steady-state fluorescence spectra were recorded on a HORIBA NanoLog spectrofluorometer. Absolute photoluminescence quantum efficiencies were determined using a HAMAMATSU PHOTONICS Quantaurus-QY Plus Absolute PL quantum yield spectrometer C13534-01.

Cyclic voltammetry (CV) and differential pulse voltammetry (DPV) measurements were performed in a three-electrode cell using an ALS 601E electrochemical analyzer in DMF containing 0.1 M tetra-*n*-butylammonium hexafluorophosphate (Bu_4NPF_6) as a supporting electrolyte. Photoemission yield spectroscopy in air (PYSA) measurements were performed using AC-3 (Riken Keiki).

2. Measurements

Photoluminescence decays. Py-Bn-MoS_2 or Py-Ph in solvent (DMF or toluene) was excited with femtosecond pulses (90 fs duration, 210 μJ cm^{-2} $pulse^{-1}$) from a femtosecond Ti:sapphire laser system (Spectra-Physics, Solstice & TOPAS Prime; 1 kHz repetition rate). The samples were photoexcited by a pulse at λ = 345 nm (2 μJ $pulse^{-1}$, 500 Hz) from TOPAS. The emitted light was collected by an off-axis parabolic mirror, dispersed in wavelength with a polychromator, and then detected by a streak camera (Hamamatsu, C14831-130). The time resolution was ca. 30 ps. The photoluminescence decay of Py-Bn-MoS_2 was almost identical when the excitation intensity was reduced to half.

Transient absorption. The picosecond transient absorption measurements were carried out by the pump-probe method with a Ti:sapphire regenerative amplifier (Spectra Physics, Solstice) and optical parametric amplifiers (OPA; Spectra Physics, TOPAS Prime). The samples were photoexcited by a pulse at λ = 345 nm (2 μJ $pulse^{-1}$, 500 Hz) from TOPAS. The transient absorption spectra were measured with a super- continuum probe generated by focusing a 1250 nm OPA signal into a 5 mm-thick BaF_2 plate. After the sample, the probe was dispersed with a polychromator and detected with a diode array (UNISOKU, PK120-C). A global analysis of the transient absorption results was performed using the GLOTARAN software[S1] with a parallel model.

3. Theoretical calculations

Py-Bn-MoS_2 model was prepared as described in the main text. Several type of edge structures are present for MoS_2 nanosheet.[S2,S3] Here the triangular structure with one sulfur atom at the edge was adopted for easy convergence of DFT calculations. The geometry of the model was first optimized in the ground state at the ωB97X-D/def2-SV(P) level. The ωB97X-D functional was adopted because it includes both the long-range correction and dispersion effect, which are required to properly describe the charge-transfer excited states and adsorption of pyrene and phenyl groups on MoS_2 surface. It is noted that although the calculated HOMO-LUMO energy gap of pyrene (Fig. 6b) is larger than the experimental one, as well as the other long-range-corrected functionals,[S4,S5] the calculated emission

energy is in good agreement with the experimental one. Then the geometry in the emission state was obtained by fitting the excited-state geometry of 1-phenylpyrene to the ground-state one. Notably, because many vacant orbitals of MoS_2 are present energetically below the LUMO of pyrene, the emission state of pyrene is very highly excited state (>100th exited state) in the whole system, making the direct geometry optimization of emission state very difficult. The emission state in DMF solution was calculated by TDDFT combined with the SMD solvation model employing the corrected linear response (cLR) approach[S6] at the ωB97X-D/def2-SV(P) level. The charge distributions of emission and ground states were obtained by reproducing the electrostatic potential according to the Merz-Singh-Kollman scheme.[S7]

To examine the solvent dependence of emission energy, the 3D-RISM calculations were performed. The Kovalenko-Hirata closure[S8] was employed to solve the 3D-RISM equation. The Lennard-Jones parameters of MoS_2 were taken from Ref. S9 whereas the others were taken from the optimized potentials for liquid simulations (OPLS) force field.[S10] The electrostatic potential distribution from solvent in the emission state was obtained for each solvent. The emission energy in each solvent, $E_{\mathrm{em}}(\mathrm{solv})$, was calculated as the difference of interaction energies from DMF solution,

$$E_{\mathrm{em}}(\mathrm{solv}) = E_{\mathrm{em}}(\mathrm{DMF}) + \Delta E_{\mathrm{int}}$$

where $E_{\mathrm{em}}(\mathrm{DMF})$ is the emission energy calculated at the cLR-SMD(DMF)-ωB97X-D/def2-SV(P) level, and

$$\Delta E_{\mathrm{int}} = \sum_i \Delta Q_i \Delta V_i$$

where ΔQ_i is the charge difference of *i*-th atom between emission and ground states, and ΔV_i is the difference in electrostatic potential from the solvent:

$$\Delta Q_i = Q_i^{\mathrm{em}} - Q_i^{\mathrm{gr}}$$

$$\Delta V_i = V_i(\mathrm{solv}) - V_i(\mathrm{DMF})$$

All the quantum chemical calculations were performed using Gaussian 16.[S11] For the 3D-RISM calculations, we used the program by Yoshida et al.[S12,S13]

4. Structure characterization of Br-Bn-MoS_2

In the FT-IR spectrum of Br-Bn-MoS_2, the signals for the C=O stretch and the S-C stretch appear, whereas that of alkene C-H bending mode is depleted (Figs. S6a and S6b). This confirms that C=C of the maleimide unit was cleaved to form C-S bonds on the MoS_2 nanosheet of Br-Bn-MoS_2. In addition, the C-H and Ar-H vibration signals were observed in the spectrum of Br-Bn-MoS_2, supporting the existences of -CH_2- and phenylene groups (Fig. S6c). Resonant Raman spectrum of Br-Bn-MoS_2 excited at 532 nm exhibits characteristic bands of MoS_2, including in-plane (E^1_{2g}), out-of-plane (A_{1g}), and S-vacancy-induced (2LA(M)) vibrations (Figs. S6d). The absence of the *J* peak series (around 155, 225, and 330 cm^{-1}) characteristic to metallic 1T MoS_2 indicate the preservation of semiconducting 2H nature of MoS_2 in Br-Bn-MoS_2.

The covalent functionalization of BM-MoS_2 with Br-Bn-mal by the solid-state reaction is also evidenced by comparing XPS patterns of BM-MoS_2 and Br-Bn-MoS_2 (Fig. S7). In the C region of Br-Bn-MoS_2, components for C=O, C-S, and C-N are needed for the appropriate fitting. In addition, the broad signal in the S 2p region of Br-Bn-MoS_2 also requires an additional component that corresponds to the S-C bond. Although the XPS patterns of Br-Bn-MoS_2 and BM-MoS_2 in the Mo region are similar, characteristic peaks for N 1s and Br 3d appear at 400.5 and 70.4 eV, respectively, in XPS of Br-Bn-MoS_2, which can be unambiguously assigned to the Br-Bn-suc moiety.

AFM and FE-SEM measurements support the nanosheet structures of Br-Bn-MoS_2 (Fig. S8). The average thickness and lateral size of Br-Bn-MoS_2 are 2.6±0.8 nm and 140±42 nm, respectively (Figs. S8b and S8c), suggesting that Br-Bn-MoS_2 mainly contains mono-layered MoS_2 nanosheets and tilted Br-Bn-suc moieties on the MoS_2 nanosheets. In addition, the energy dispersive X-ray (EDX) spectroscopy map of Br-Bn-MoS_2 revealed the distributed feature of Br all around the MoS_2 nanosheet (Fig. S9). This result indicates that Br-Bn-suc groups are not localized at the edges of the MoS_2 nanosheet of Br-Bn-MoS_2 but homogeneously attached onto the surface.

TGA of Br-Bn-MoS_2 showed a weight decrease at 400–600 °C (Fig. 2a), which corresponds to the detachment of the Br-Bn-suc group. A clear weight loss was not observed in the TGA curve of Br-

Bn-MoS_2 at 200–270 °C, which is the thermal decomposition temperature of Br-Bn-mal. In addition, the further washing of the Br-Bn-MoS_2 sample with acetonitrile did not change the TGA curve. These results suggest the complete removal of physisorbed and intercalated Br-Bn-mal molecules out of Br-Bn-MoS_2. From the difference in the relative weights of BM-MoS_2 and Br-Bn-MoS_2 at 600 °C, the weight ratio of Br-Bn-suc moieties in Br-Bn-MoS_2 is estimated to be 40wt%. This corresponds to 1 Br-Bn-suc unit in every 5 S atoms. To check whether this functionalization ratio is sterically possible or not, a model of Br-Bn-MoS_2 was constructed by attaching 10 Br-Bn-suc units onto 5 S atoms in the top and bottom surfaces, respectively, of a small molybdenum disulfide nanosheet ($Mo_{28}S_{63}$) (Fig. S10). The functionalization ratio of this model matches well with that of the experimentally obtained Br-Bn-MoS_2 (see the caption of Fig. S10). The space-filling model in Fig. S10a suggests that this functionalization ratio, i.e., one out of five S atoms has a Br-Bn-suc unit, is sterically possible.

5. Materials

N-(4-Bromobenzyl)maleimide and 1-phenylpyrene were synthesized according to the reported procedure.[S14,S15] Bulk MoS_2 (<98%) was purchased from Sigma–Aldrich. All other chemicals and solvents were purchased from commercial supplier and used without further purification.

6. Synthetic procedure

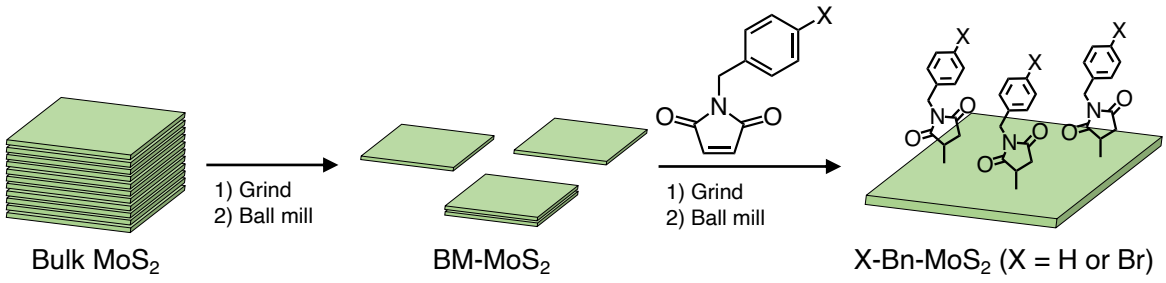

BM-MoS_2. Under an argon atmosphere, bulk MoS_2 grainy powder (600 mg) was ground into fine powder in an agate mortar. Then, the MoS_2 powder and 50 Si_3N_4 balls with a diameter of 5 mm were added to a Si_3N_4 ball-milling container (12 mL). Exfoliation was conducted using a planetary ball-

milling system for 24 h (30 min milling, 15 min pause, 32 cycles) at 500 rpm. Fine powder of ball-milled MoS_2, BM-MoS_2, was collected (400 mg) and kept under an argon atmosphere.

X-Bn-MoS_2 (X = H or Br). A typical procedure for the preparation of H-Bn-MoS_2 and Br-Bn-MoS_2 was as follows. Under an argon atmosphere, granule of a maleimide derivative (*N*-benzylmaleimide (H-Bn-mal) or *N*-(4-bromobenzyl)maleimide (Br-Bn-mal), 500 mg) was ground into fine powder in an agate mortar. Then, BM-MoS_2 powder (200 mg) was added into the agate mortar and mixed with the maleimide derivative. The mixed powder and 50 Si_3N_4 balls with a diameter of 5 mm were then added to a Si_3N_4 ball-milling container (12 mL), and the solid-state reaction was conducted using a planetary ball-milling system for 24 h (30 min milling, 15 min pause, 32 cycles) at 500 rpm. After collecting the resultant powder into a vial container under an ambient atmosphere, acetonitrile was added. Then, the mixture was sonicated for 10 min using a bath sonicator and filtered through a PTFE membrane (0.1 μm). The product was washed thoroughly with acetonitrile by the repeated sonication and filtration to remove the excess maleimide derivative. The resulting solid was dried under vacuum overnight to yield X-Bn-MoS_2 (X = H or Br) as a dark gray powder (typically, 200 mg).

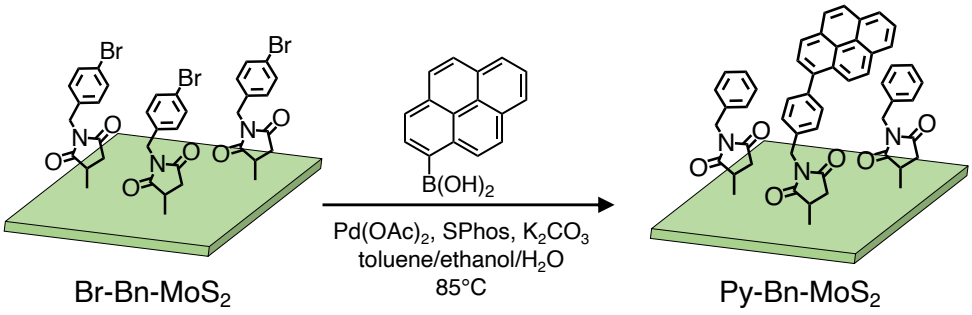

Py-Bn-MoS_2. A flask was charged with Br-Bn-MoS_2 (33.0 mg), 1-pyreneboronic acid (44.0 mg, 0.179 mmol), $Pd(OAc)_2$ (1.9 mg, 0.0085 mmol), SPhos (3.8 mg, 0.0094 mmol), toluene (2.0 mL), ethanol (0.6 mL), and 2M K_2CO_3 (0.27 mL, 0.54 mmol) under an argon atmosphere. After sonication for 5 min and bubbling with argon for 5 min, the reaction mixture was stirred for 3 days at 85 °C under protection from light. Then, 1-pyreneboronic acid (44.0 mg, 0.179 mmol), $Pd(OAc)_2$ (1.9 mg, 0.0085 mmol), SPhos (3.8 mg, 0.0094 mmol), toluene (2.0 mL), ethanol (0.6 mL), and 2M K_2CO_3 (0.27 mL, 0.54 mmol) were added to the reaction mixture. After sonication and Ar-bubbling, the reaction mixture was again stirred for 2 days at 85 °C under protection form light. Furthermore, 1-

pyreneboronic acid (22.0 mg, 0.0894 mmol) was added to the reaction mixture, which was subsequently sonicated, Ar-bubbled, and stirred for 2 days at 85 °C under protection from light. After cooling to room temperature, the mixture was diluted with diethyl ether, sonicated for 10 min, and filtered through a PTFE membrane (0.1 μm). The product was washed thoroughly with diethyl ether, water, and acetone, in this order to remove residual pyrene compounds. The resulting solid was dried under vacuum overnight to yield Py-Bn-MoS_2 as a gray powder (20 mg).

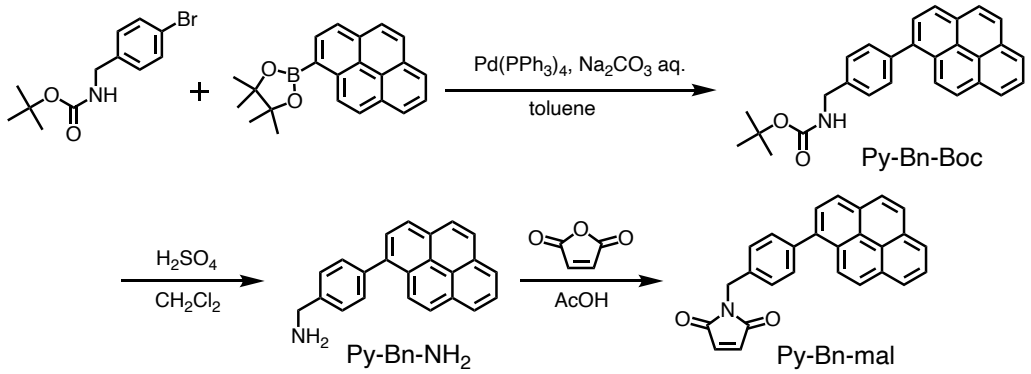

4-(1-Pyrenyl)-*N*-Boc-benzylamine (Py-Bn-Boc). After degassing a mixture of 1-pyreneboronic acid pinacol ester (0.33 g, 1.0 mmol), 4-bromo-*N*-Boc-benzylamine (0.29 g, 1.0 mmol), toluene (20 mL), and aqueous sodium carbonate solution (1.0 M, 10 mL), $Pd(PPh_3)_4$ (23.0 mg, 2 mol%) was added and the mixture was stirred under reflux for 20 h at 120 °C. The layers were then separated, the aqueous phase was extracted with toluene (30 mL, 3 times), the combined organic phases were dried with Na_2SO_4, and the solvent was evaporated. The residue was purified by silica column chromatography with CH_2Cl_2/hexane = 1: 2 as eluent. Py-Bn-Boc was obtained as a pale orange solid (0. 32 g, yield: 82%). ^{1}H NMR (400 MHz, $CDCl_3$): δ 8.23-7.95 (9H), 7.60 (d, J = 7.6 Hz, 2H), 7.48 (d, J = 7.6 Hz, 2H), 4.47 (d, J = 5.6 Hz, 2H), 4.98 (s, 1H), 1.51 (s, 9H). ^{13}C NMR (100 MHz, $CDCl_3$, ppm): δ 155.59, 140,26 137.94, 137.30, 131.66, 131.47, 130.94, 130.82, 130.58, 128.48, 127.56, 127.48, 127.40, 126.02, 125.19, 125.12, 124.93, 124.83, 124.64, 79.63, 44.51, 28.46. HRMS (APCI) calcd for $[C_{27}H_{17}NO_2]^+$: 407.5032; found 407.4820. IR (ATR, cm^{-1}): ν_{max} 3881, 3745, 3735, 3676, 3629, 3422, 3355, 3046, 2977, 2931, 1696, 1653, 1603, 1456, 1390, 1365, 1271, 1252, 1168, 1072, 1047, 1023, 934, 847, 819, 794, 758, 721, 683, 615, 598, 581, 556, 490, 468, 458, 447, 438, 428, 418, 406, 403.

4-(1-Pyrenyl)-benzylamine (Py-Bn-NH_2). The reaction was carried out by adding dropwise the mixture consisting of 96% H_2SO_4 (6.0 mmol) and CH_2Cl_2 (5.0 mL) into a chilled, well stirred solution of Py-Bn-Boc (1.59 g 4.0 mmol) in CH_2Cl_2 (15 mL), and stirring the resulting mixture for 6 h at room temperature. After this time, the reaction was quenched with 4.0 M NaOH (20 mL), and extracted with CH_2Cl_2 (20 mL, 2 times) and then the organic phase was dried over Na_2SO_4. After filtration, the solvent was removed under reduced pressure. The crude product was obtained as yellow solid and used in the next step without further purification.

4-(1-Pyrenyl)-*N*-benzylmaleimide (Py-Bn-mal). Maleic anhydride (0.35 g, 3.57 mmol, 1.05 equiv.) and Py-Bn-NH_2 (less than 3.4 mmol, 1.0 equiv.) and copper(II) dibutyldithiocarbamate (2.9 mg, 0.0061 mmol) were stirred in acetic acid (10 mL) until maleic anhydride dissolved completely. The reaction mixture was then refluxed overnight at 140 °C. After completion of the reaction, the reaction mixture was allowed to cool down to room temperature and the whole reaction mixture was transferred to a 500 mL flask. Saturated sodium bicarbonate aqueous solution was added to the flask containing reaction mixture until effervescence stopped. The aqueous mixture was extracted with dichloromethane (200 mL, 3 times). The organic layer was further washed with 1.0 M HCl (100 mL, 2 times) and then the organic phase was dried over Na_2SO_4. After filtration, the solvent was removed under reduced pressure and the residue was purified by silica column chromatography with CH_2Cl_2/hexane = 1:2 as eluent. Py-Bn-mal was obtained as yellow solid (0.65 g, yield: 49%). ^{1}H NMR (400 MHz, $CDCl_3$, ppm): δ 8.22-7.93(9H), 7.59 (d, J = 8.4 Hz, 2H), 7.54 (d, J = 7.6 Hz, 2H), 6.79 (s, 2H) 4.83 (s, 2H). ^{13}C NMR (100 MHz, $CDCl_3$, ppm): δ 170.54, 140.80, 137.06 135.12, 134.31, 131.43, 130.91, 130.61, 128.41, 127.52, 127.37, 126.03, 125.14, 124.86, 124.63, 41.24. HRMS (APCI) calcd for $[C_{27}H_{17}NO_2+H]^+$: 388.1338; found 388.1338. IR (ATR, cm^{-1}): ν_{max} 3087, 3037, 2938, 2355, 2340, 1739, 1699, 1602, 1498, 1437, 1401, 1396, 1336, 1326, 1141, 1106, 1034, 882, 852, 830, 757, 751, 696, 693, 621, 620, 565, 540, 502, 501, 446.

7. Supplementary tables

Table S1 Absorption and photoluminescence maxima (λ_{abs} and λ_{PL}) and Stokes shift of Py-Bn-MoS_2 in various solvents

Solvent	λ_{abs} / nm	λ_{PL} / nm	Stokes shift / cm^{-1}
benzene (BZ)	349	427	5230
toluene (TOL)	348	426	5260
chloroform (CLF)	348	439	5960
dichloromethane (DCM)	347	444	6300
benzonitrile (BN)	346	456	6970
DMF	348	453	6660
DMSO	347	452	6700

Table S2 Wavelengths of positive peaks (λ_P) and negative peaks (λ_N) in transient absorption decay component spectra of Py-Bn-MoS_2 in DMF (Fig. 4f) and toluene (Fig. S16g) obtained with global three-component fit of the data

component	DMF		toluene	
	λ_P / nm	λ_N / nm	λ_P / nm	λ_N / nm
1st	577, 642, 711, 924	618, 674, 875, 947	584, 648, 712	543, 624, 679, 895
2nd	490, 640, 694, 818	600, 659, 797, 891	650, 714	619, 670, 892
3rd	497, 621, 860	600, 656	563, 639, 892	598, 654

Table S3 Emission energies (E_{em}) and wavelengths (λ_{em}) of pyrene and Py-Bn-MoS_2 model in various solvents[a]

solvent	pyrene		Py-Bn-MoS_2 model	
	E_{em} / eV	λ_{em} / nm	E_{em} / eV	λ_{em} / nm
no solvent	3.66	339	3.03	409
benzene (BZ)	3.67	338	2.97	417
toluene (TOL)	3.67	338	2.94	422
chloroform (CLF)	3.67	338	2.85	435
dichloromethane (DCM)	3.67	338	2.80	443
benzonitrile (BN)	3.67	338	2.76	449
DMSO	3.67	338	2.71	458
DMF	3.67	338	2.67	464

[a]All the values were obtained using the 3D-RISM method based on charge distributions calculated cLR-SMD(DMF)-ωB97X-D/def2-SV(P) level.

8. Supplementary figures

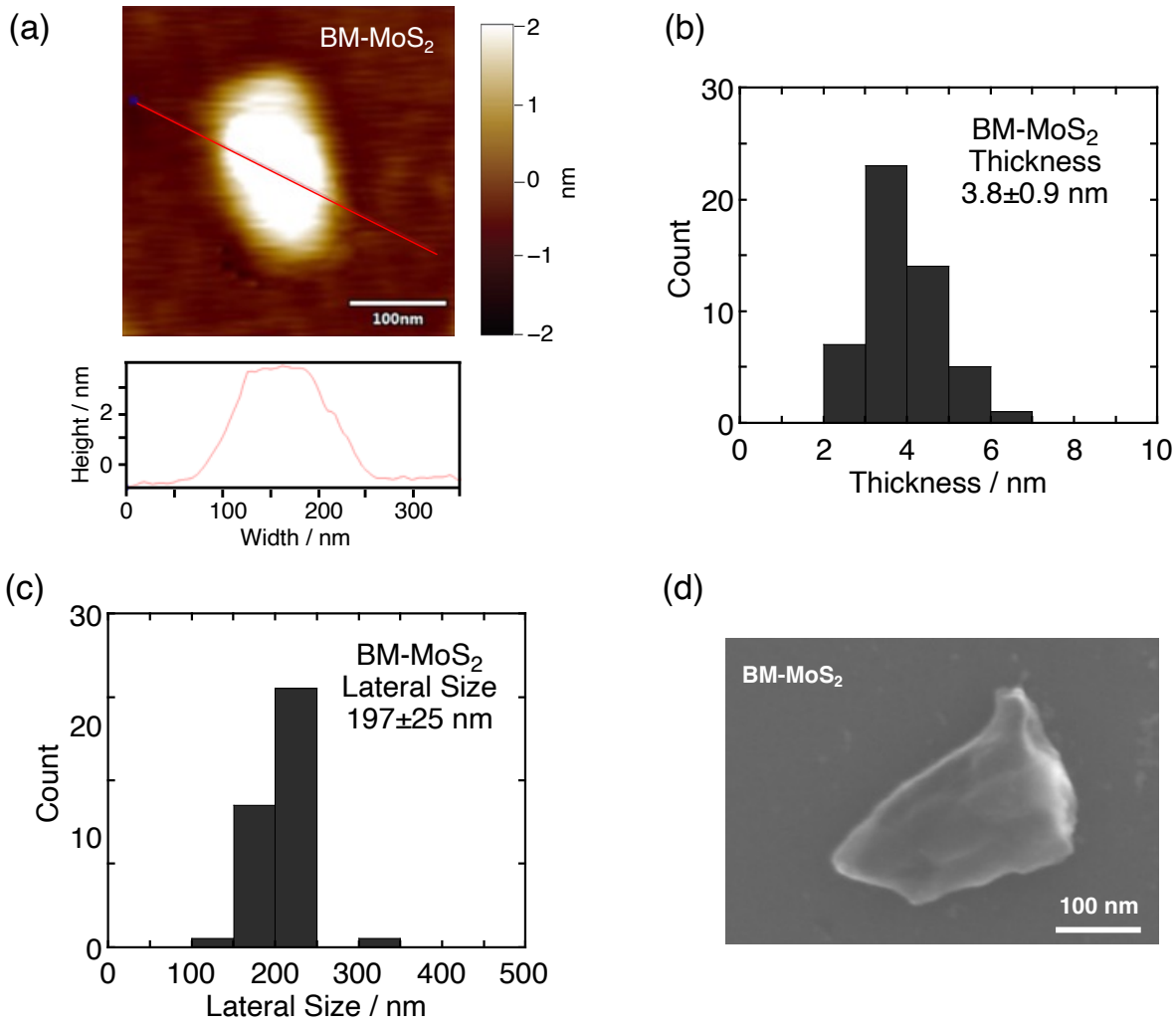

Fig. S1 (a) AFM image with section profile of BM-MoS_2 spin coated on a mica from NMP dispersion. The color scale represents the height topography, with light and dark representing the highest and lowest features, respectively. (b) Thickness and (c) lateral size distributions of BM-MoS_2 estimated by AFM measurements. 50 individual sheets were analyzed. (d) FE-SEM image of BM-MoS_2. The sample was prepared by casting the NMP dispersion onto a silicon wafer.

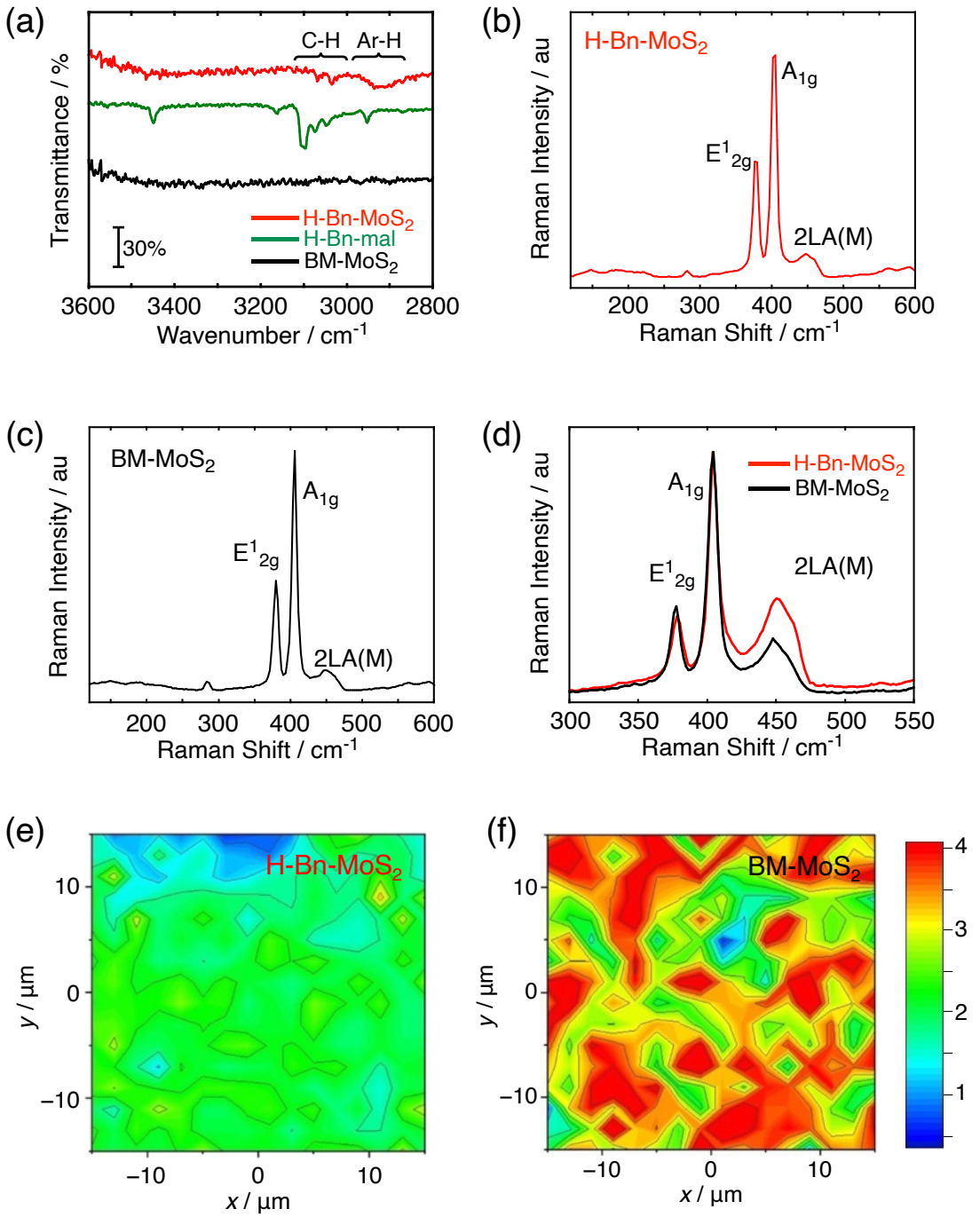

Fig. S2 (a) FT-IR spectra of H-Bn-MoS_2 (red), H-Bn-mal (green), and BM-MoS_2 (black) with the region of 3600–2800 cm^{-1}. (b,c) Resonant Raman spectra of (b) H-Bn-MoS_2 and (c) BM-MoS_2 with an excitation wavelength of 532 nm. (d) Resonant Raman spectra of H-Bn-MoS_2 (red) and BM-MoS_2 (black) with an excitation wavelength of 633 nm. The spectra are averaged from the measurements of 256 points, respectively. The Raman intensities are normalized at the A_{1g} peaks. (e,f) Raman mapping, upon excitation at 633 nm, of the $I_{A1g}/I_{2LA(M)}$ intensity ratio of a 30 μm × 30 μm area for (e) H-Bn-MoS_2 and (f) BM-MoS_2.

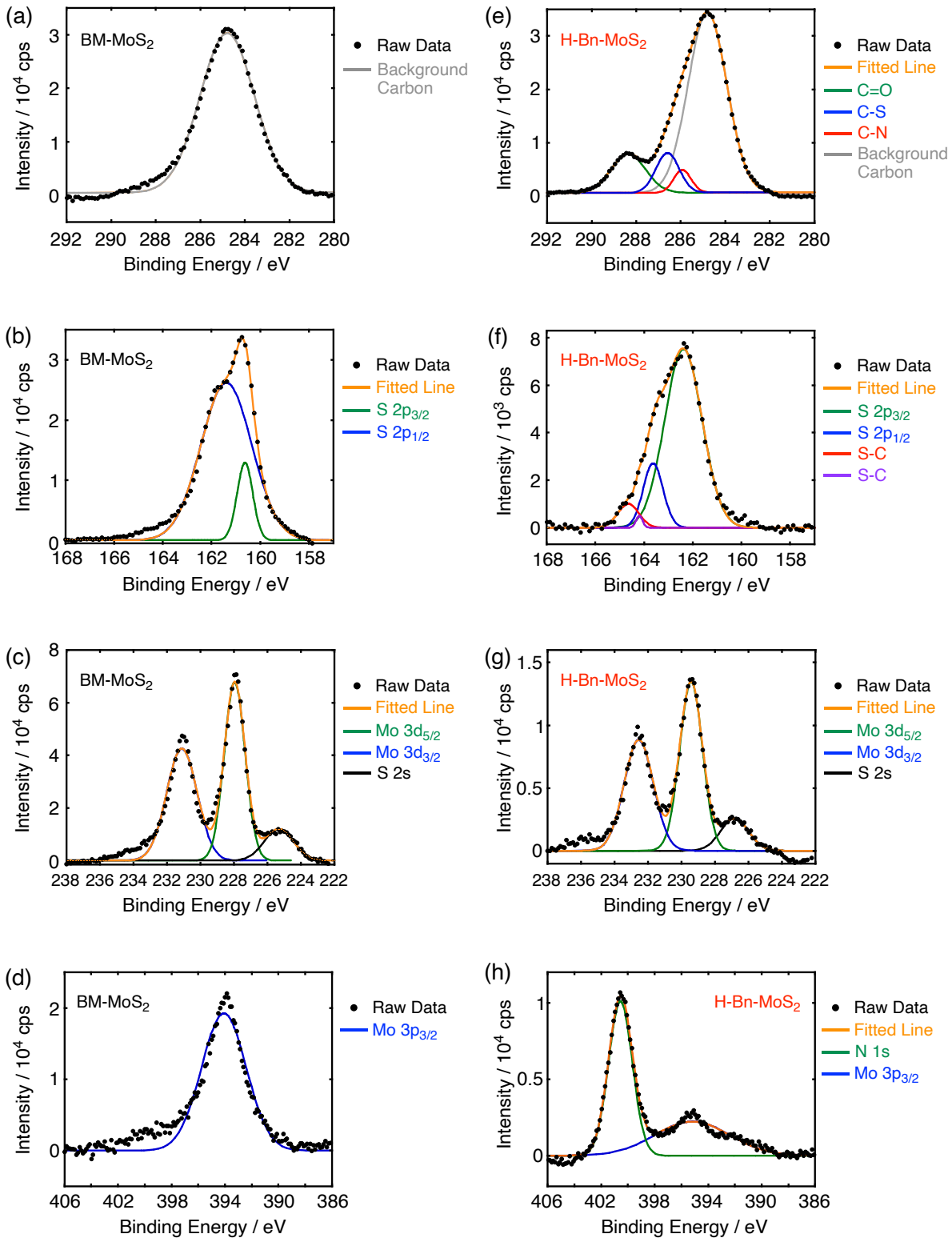

Fig. S3 XPS of C, S, Mo, and N core levels for (a–d) BM-MoS_2, and (e–h) H-Bn-MoS_2.

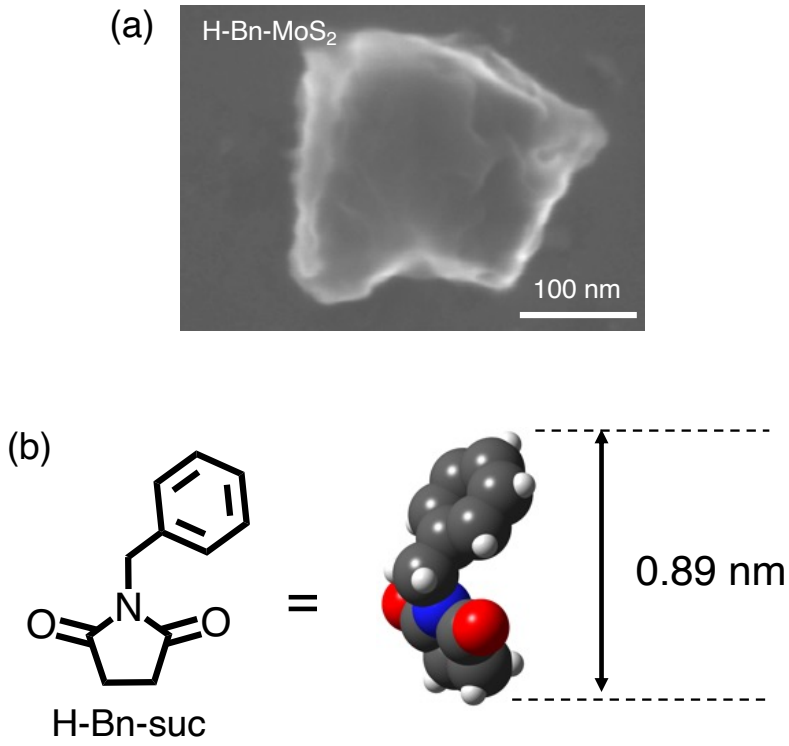

Fig. S4 (a) FE-SEM image of H-Bn-MoS_2. The sample was prepared by casting the NMP dispersion onto a silicon wafer. (b) Structure of *N*-benzylsuccinimide (H-Bn-suc) optimized by DFT using B3LYP/6-31G(d). The height of H-Bn-suc is estimated to be 0.89 nm.

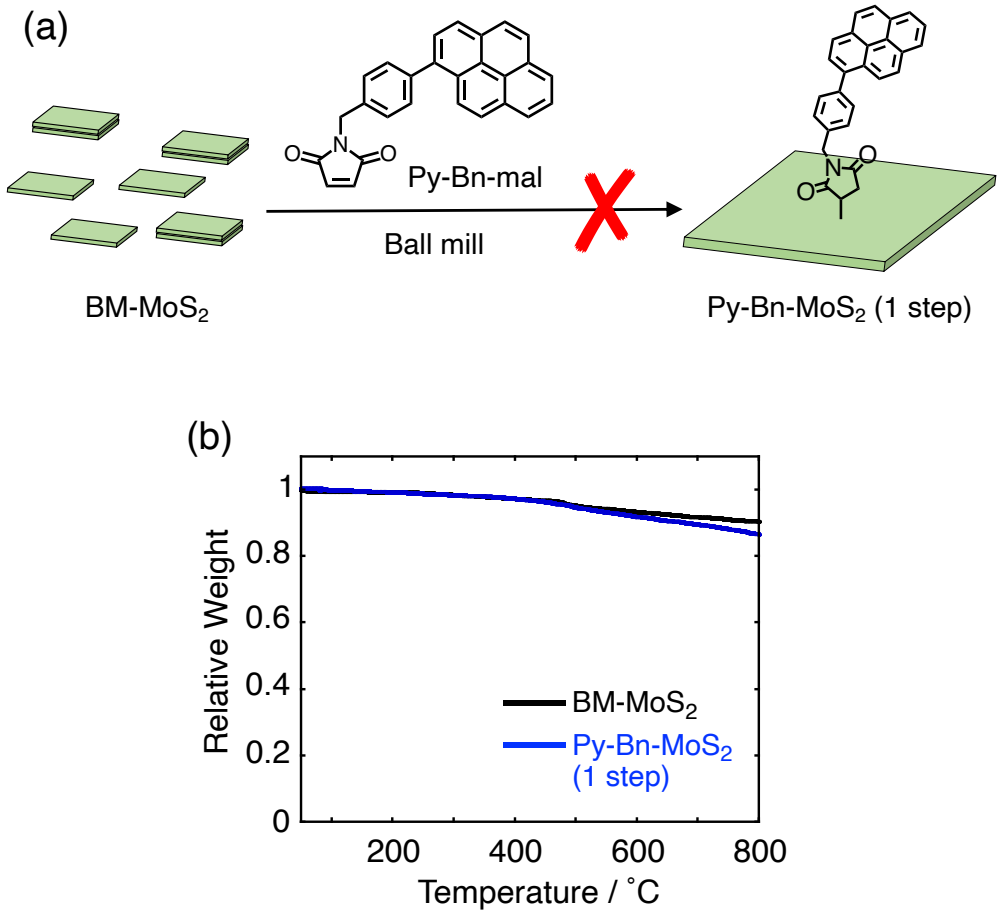

Fig. S5 (a) One step functionalization of BM-MoS_2 by Py-Bn-mal to obtain pyrene-linked MoS_2 by the ball-mill method. (b) TGA of BM-MoS_2 (black) and Py-Bn-MoS_2 prepared by the one step functionalization in (a) after thorough washing (blue). The analyses were performed under nitrogen with a heating rate of 10 °C min^{-1}. The accordance of the black and blue lines indicates that the functionalization reaction did not occur.

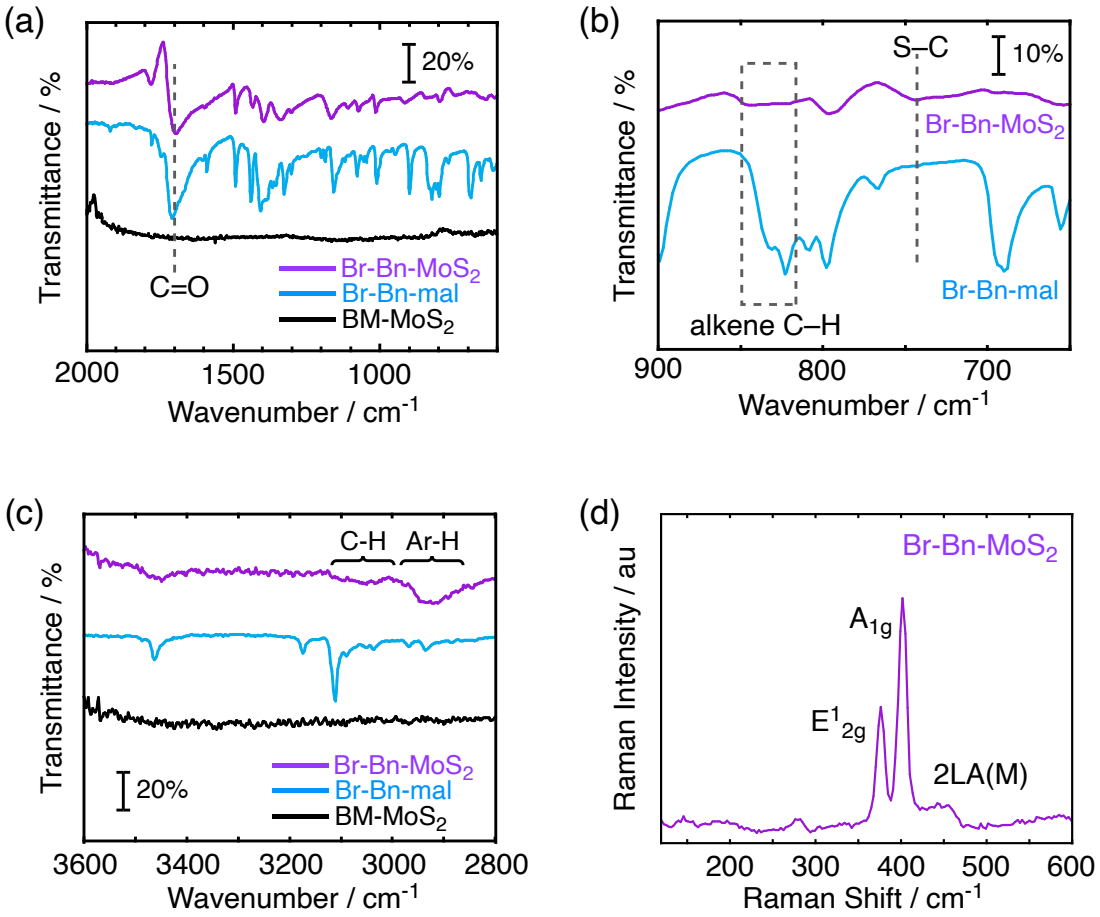

Fig. S6 FT-IR spectra of Br-Bn-MoS_2 (purple), Br-Bn-mal (light blue), and BM-MoS_2 (black) with the regions of (a) 2000–600 cm^{-1}, (b) 900–650 cm^{-1}, and (c) 3600–2800 cm^{-1}. (d) Resonant Raman spectrum of Br-Bn-MoS_2 with an excitation wavelength of 532 nm.

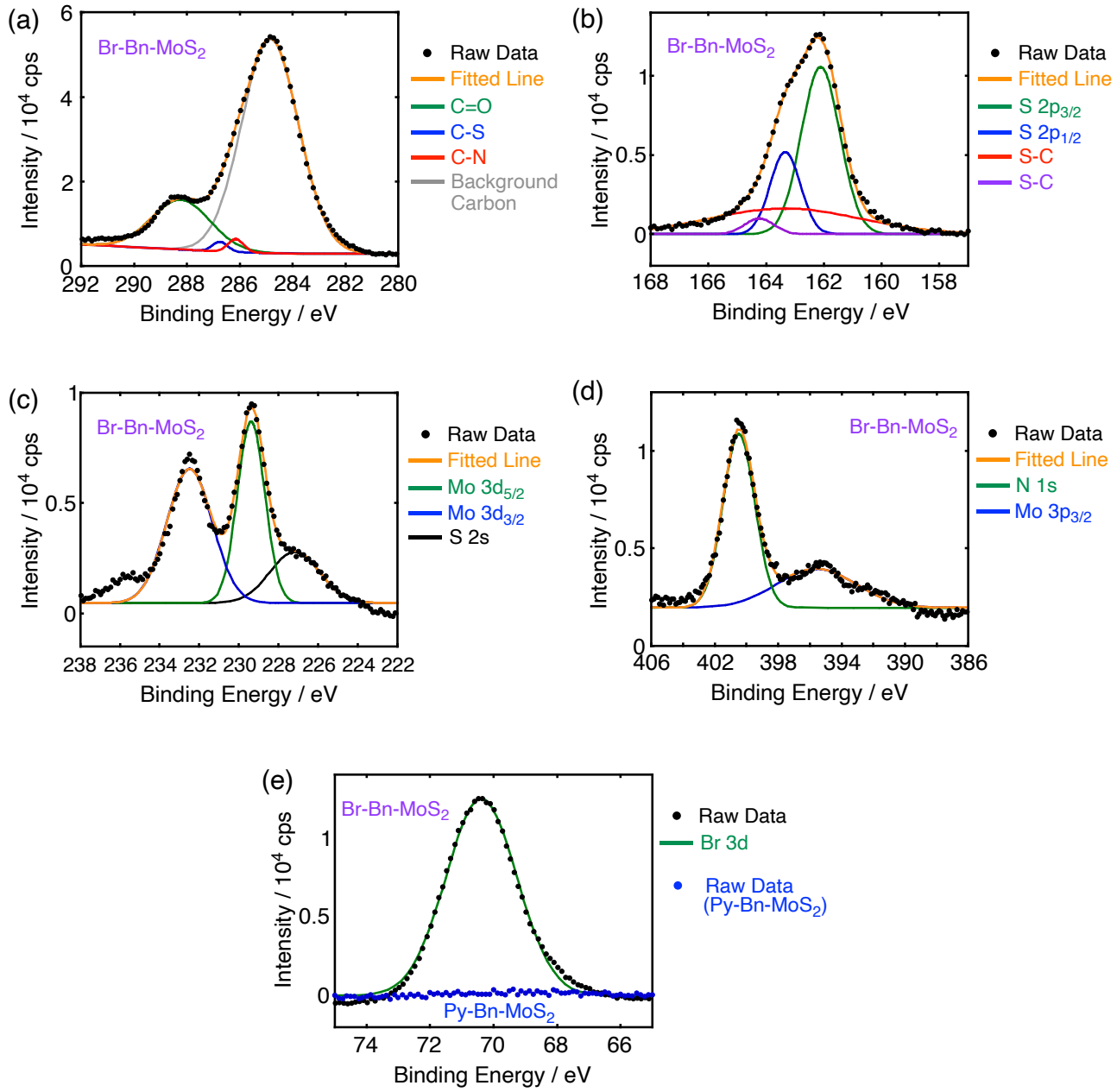

Fig. S7 XPS of (a) C, (b) S, (c) Mo, (d) N, and (e) Br core levels for Br-Bn-MoS_2. In (e), XPS of Br core levels for Py-Bn-MoS_2 is also shown.

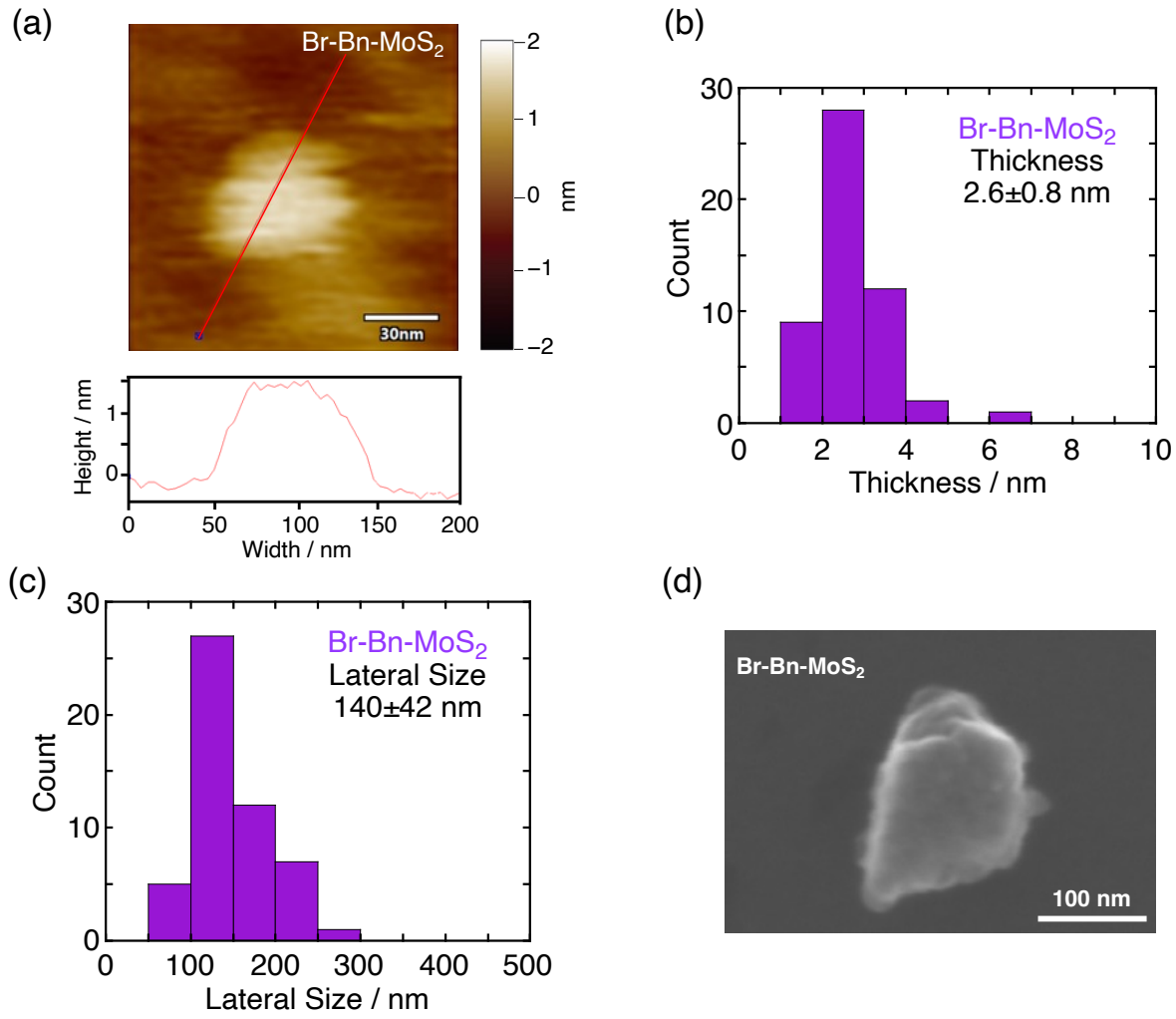

Fig. S8 (a) AFM image with section profile of Br-Bn-MoS_2 spin coated on a mica from NMP dispersion. The color scale represents the height topography, with light and dark representing the highest and lowest features, respectively. (b) Thickness and (c) lateral size distributions of Br-Bn-MoS_2 estimated by AFM measurements. 50 individual sheets were analyzed. (d) FE-SEM image of Br-Bn-MoS_2. The sample was prepared by casting the NMP dispersion onto a silicon wafer.

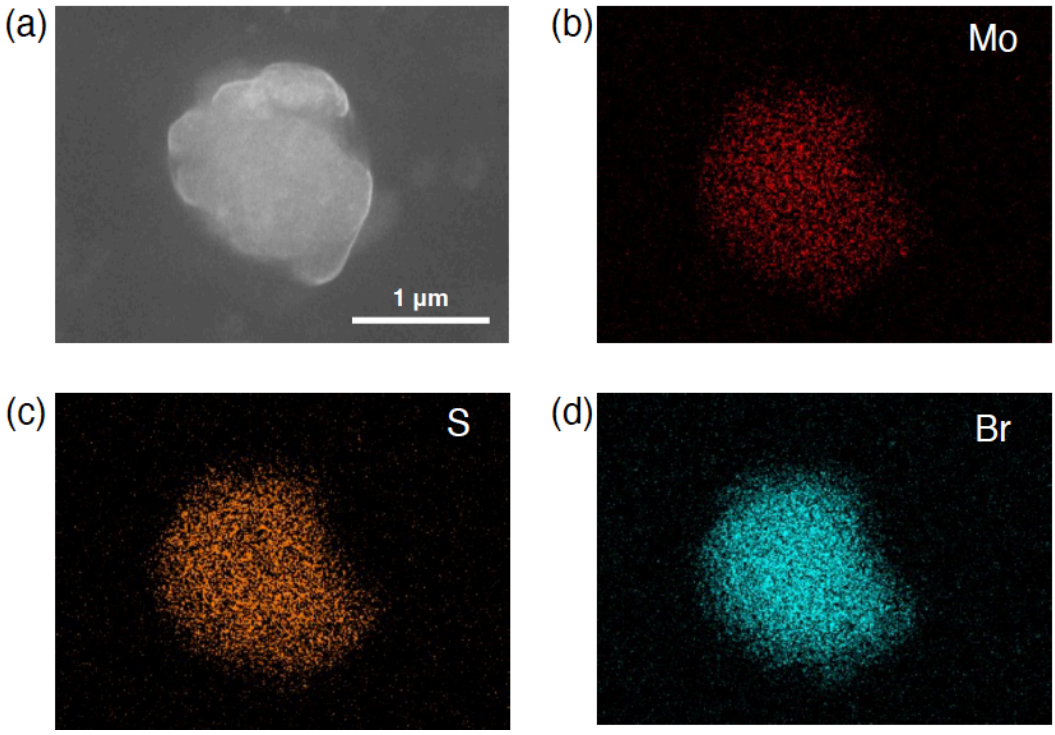

Fig. S9 (a) FE-SEM images of Br-Bn-MoS_2 with EDX maps of (b) Mo, (c) S, and (d) Br, showing the elemental distributions. The sample was prepared by putting the Br-Bn-MoS_2 powder on a conductive carbon tape. To obtain clear EDX map images, a relatively large aggregate of Br-Bn-MoS_2 with lateral size of ca. 1 μm was picked up.

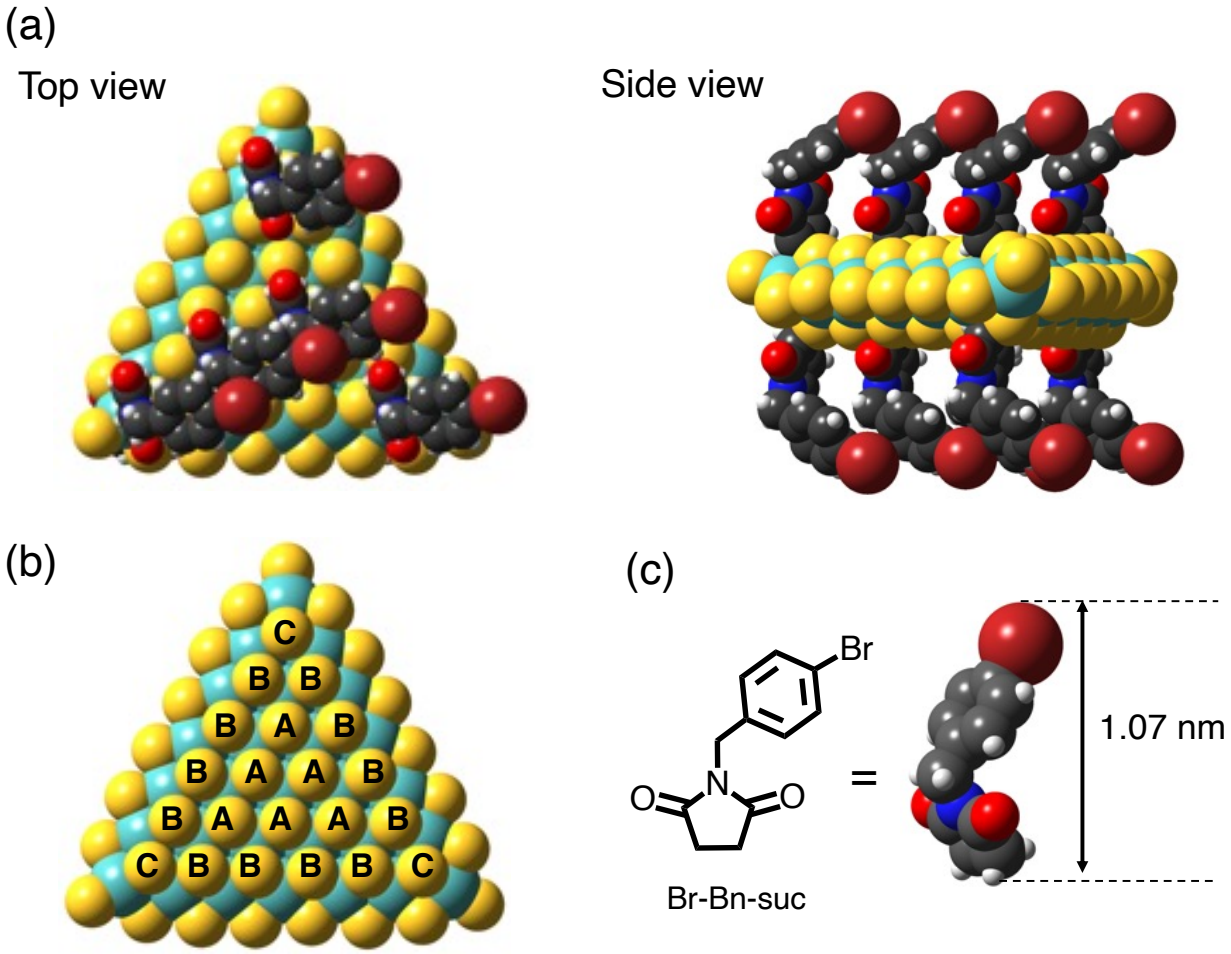

Fig. S10 (a) Top and side views of Br-Bn-MoS_2 model. (b) Top view of molybdenum sulfide model ($Mo_{28}S_{63}$) optimized by DFT using ωB97X-D/def2-SV(P). (c) Structure of *N*-*p*-bromobenzylmaleimide (Br-Bn-suc) optimized by DFT using B3LYP/6-31G(d). In the top and bottom surfaces of $Mo_{28}S_{63}$ in (b), there are planar triangles which consist of 21 S atoms. Assuming that these S triangle layers with the Mo inner layer are a unit structure and a large MoS_2 nanosheet is constructed by the 2-dimensional repetition of the unit structure, the S atoms marked with A, B, and C in (b) are shared by 1, 2, and 6 triangles, respectively, in the large MoS_2 nanosheet. In (a), 2 and 3 Br-Bn-suc units are attached to S atoms marked with A and C, respectively, on the top and bottom surfaces. This corresponds to 2.5 Br-Bn-suc units exist on 12.5 S atoms, that is, 1 Br-Bn-suc unit in every 5 S atoms of MoS_2 nanosheet.

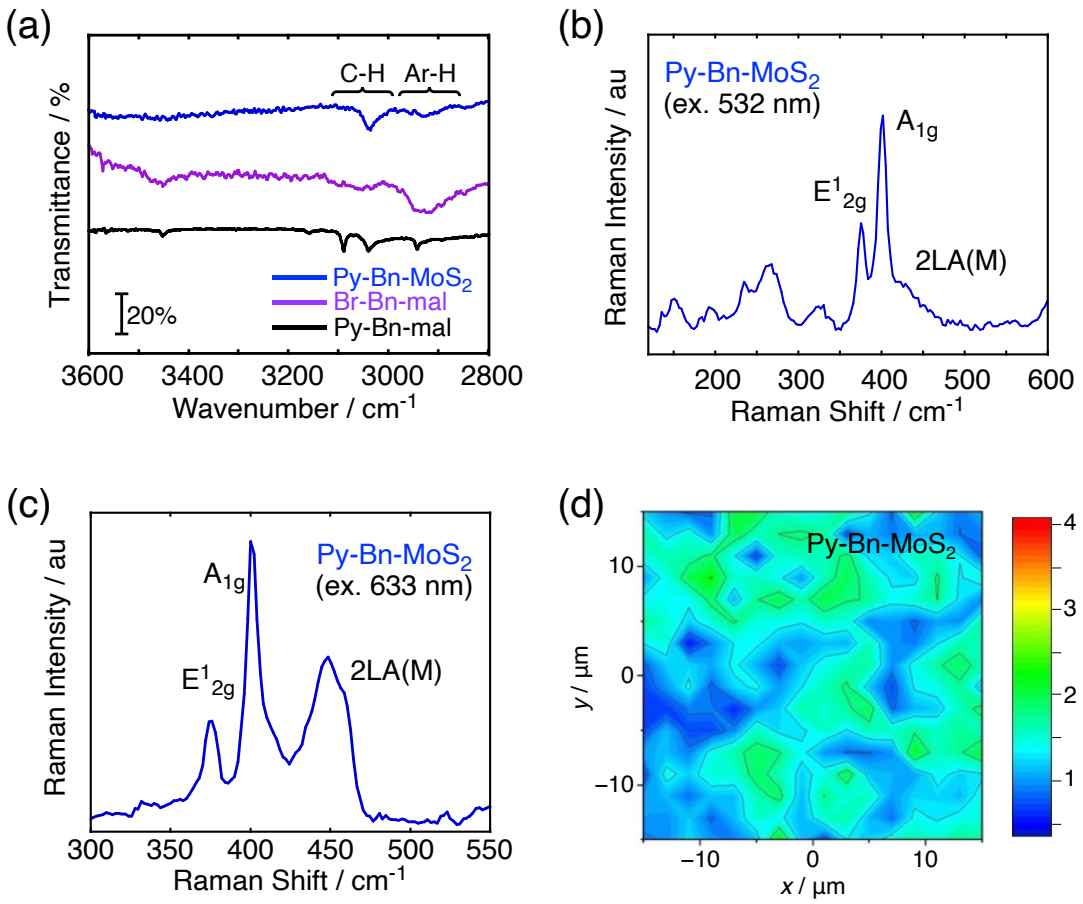

Fig. S11 (a) FT-IR spectra of Py-Bn-MoS_2 (blue), Br-Bn-MoS_2 (purple), and Py-Bn-mal (black) with the regions of 3600–2800 cm^{-1}. The C-H and Ar-H vibration signals were observed in the spectrum of Py-Bn-MoS_2, supporting the existences of -CH_2- and aromatic groups. (b,c) Resonant Raman spectrum of Br-Bn-MoS_2 with an excitation wavelength of (b) 532 nm and (c) 633 nm. The spectrum in (c) is averaged from the measurements of 256 points. (d) Raman mapping, upon excitation at 633 nm, of the $I_{A1g}/I_{2LA(M)}$ intensity ratio of a 30 μm × 30 μm area for Py-Bn-MoS_2.

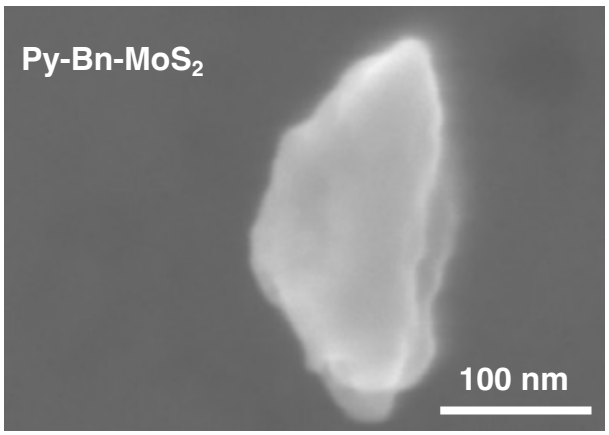

Fig. S12 FE-SEM image of Py-Bn-MoS_2. The sample was prepared by casting the NMP dispersion onto a silicon wafer.

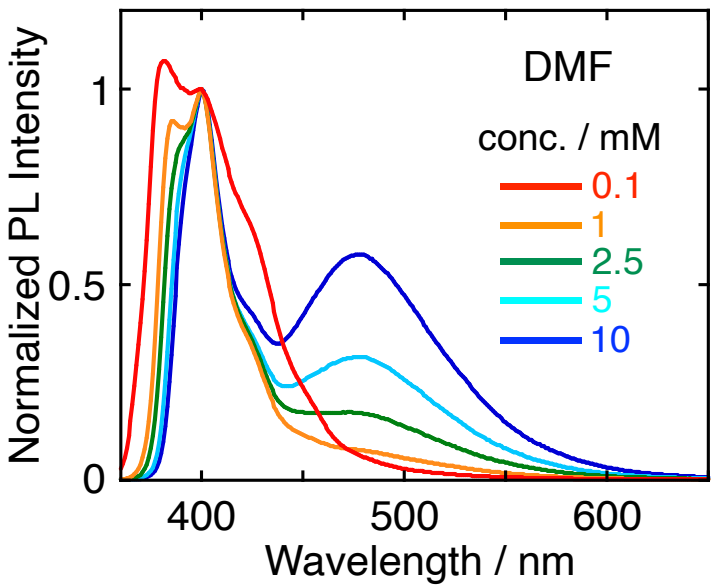

Fig. S13 Photoluminescence (PL) spectra of Py-Ph with various concentrations (0.1–10 mM) in DMF excited at 345 nm. The PL intensities are normalized at 400 nm. Py-Ph clearly shows the excimer emission around 480 nm at high concentrations.

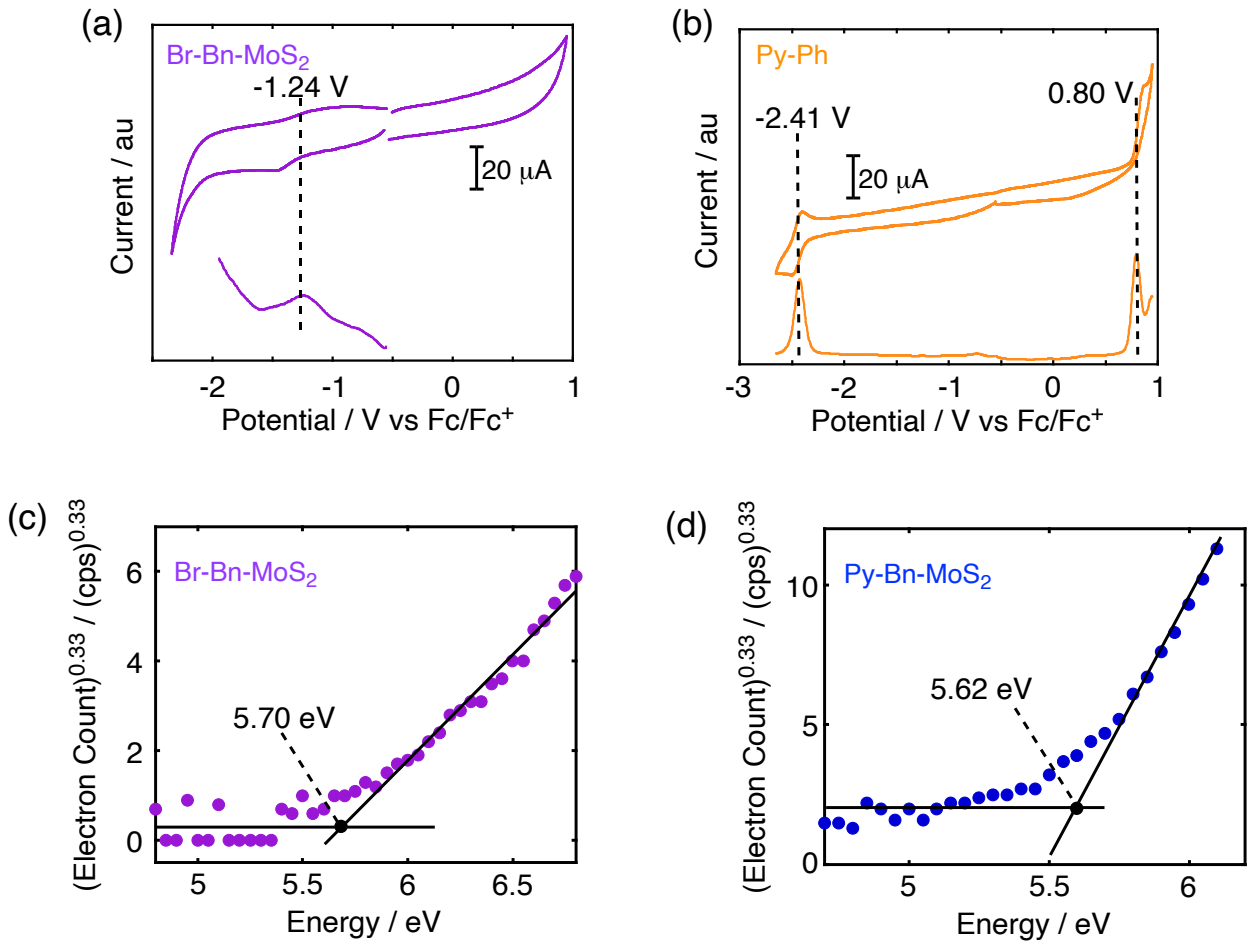

Fig. S14 (a,b) Cyclic voltammograms (CVs) and differential pulse voltammograms (DPVs) of (a) Br-Bn-MoS_2 and (b) Py-Ph in DMF containing 0.1 M Bu_4NPF_6. Sweep rate: 0.1 V s^{-1} for CV and 0.02 V s^{-1} for DPV, reference electrode: Ag/AgCl (sat. KCl), counter electrode: Pt wire, working electrode: Pt in (a) and glassy carbon in (b). (c,d) Photoemission yield spectroscopy in air (PYSA) of (c) Br-Bn-MoS_2 and (d) Py-Bn-MoS_2.

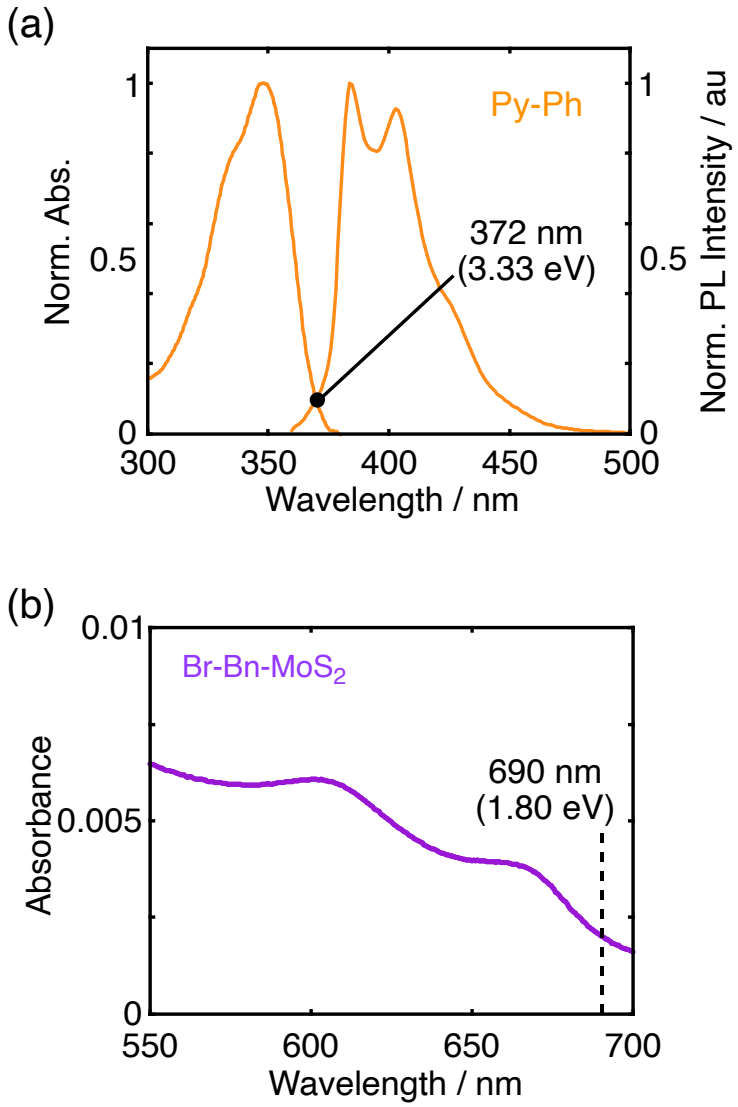

Fig. S15 (a) Normalized UV–visible absorption and fluorescence spectra of Py-Ph in DMF excited at 345 nm). The wavelength and energy at the intersection point are shown in the figure. (b) Visible absorption spectrum of Br-Bn-MoS_2 in DMF in the region of 550–700 nm. The wavelength and energy at the absorption edge of the A excitonic transition are shown in the figure.

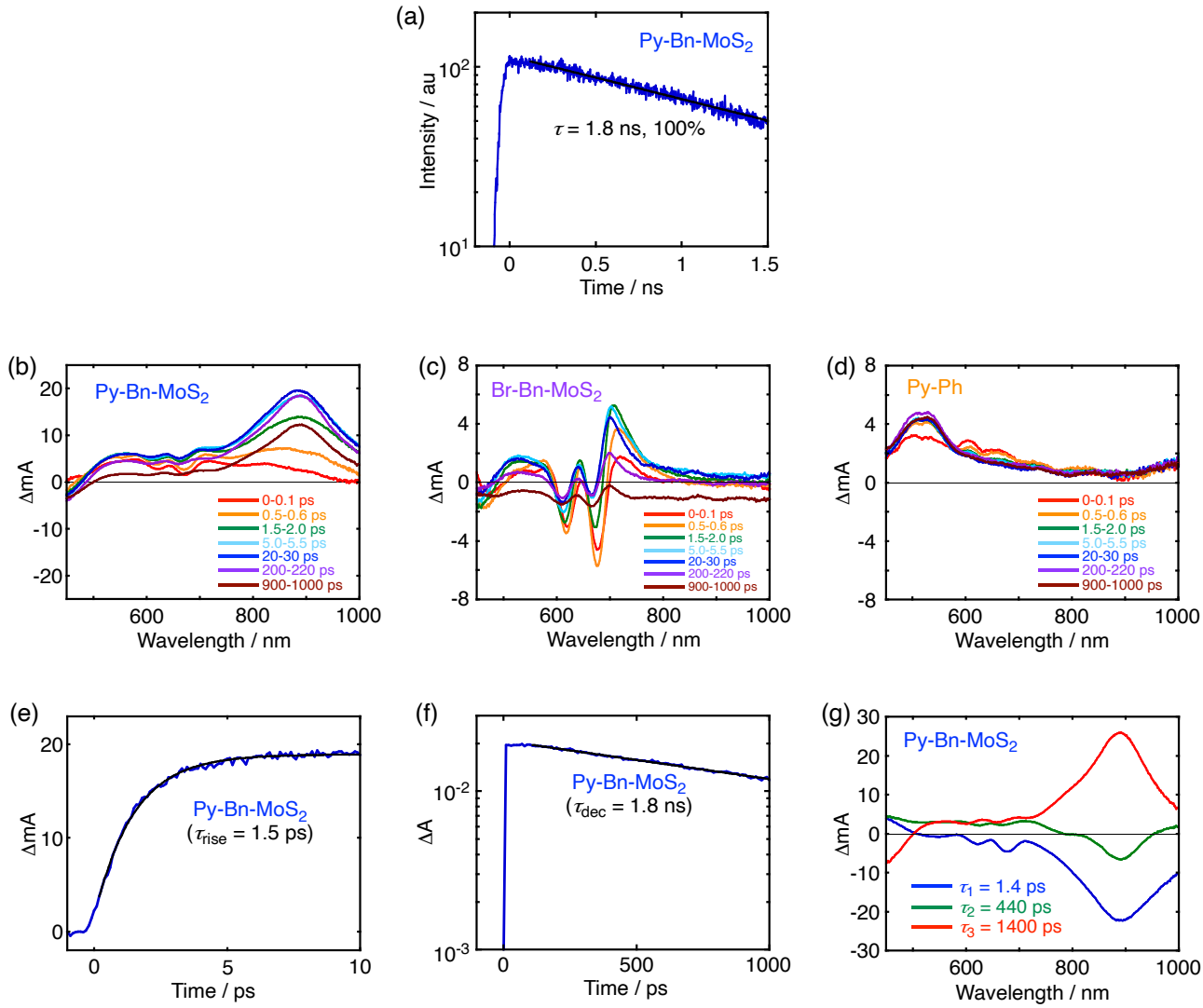

Fig. S16 (a) Photoluminescence decay of Py-Bn-MoS_2 with a fitting line (black line) in toluene measured by streak camera with time ranges of up to 1.5 ns. The excitation wavelength was 345 nm. The emission was detected at 460±10 nm. The emission lifetime (τ) and ratio are also shown in the figure. (b-d) Transient absorption spectra of (b) Py-Bn-MoS_2, (c) Br-Bn-MoS_2, and (d) Py-Ph in toluene. The excitation wavelength was 345 nm. (e,f) Transient absorption profiles of Py-Bn-MoS_2 with fitting curves (black line) in toluene with time ranges of up to (e) 10 ps and (f) 1000 ps. The excitation and detection wavelengths were 345 and 850 nm, respectively. The decay or rise lifetimes are given in the parentheses. (g) Transient absorption component spectra of Py-Bn-MoS_2 in toluene obtained with global three-component fit of the data. The excitation wavelength was 345 nm. The lifetimes of respective components are given in the figure.

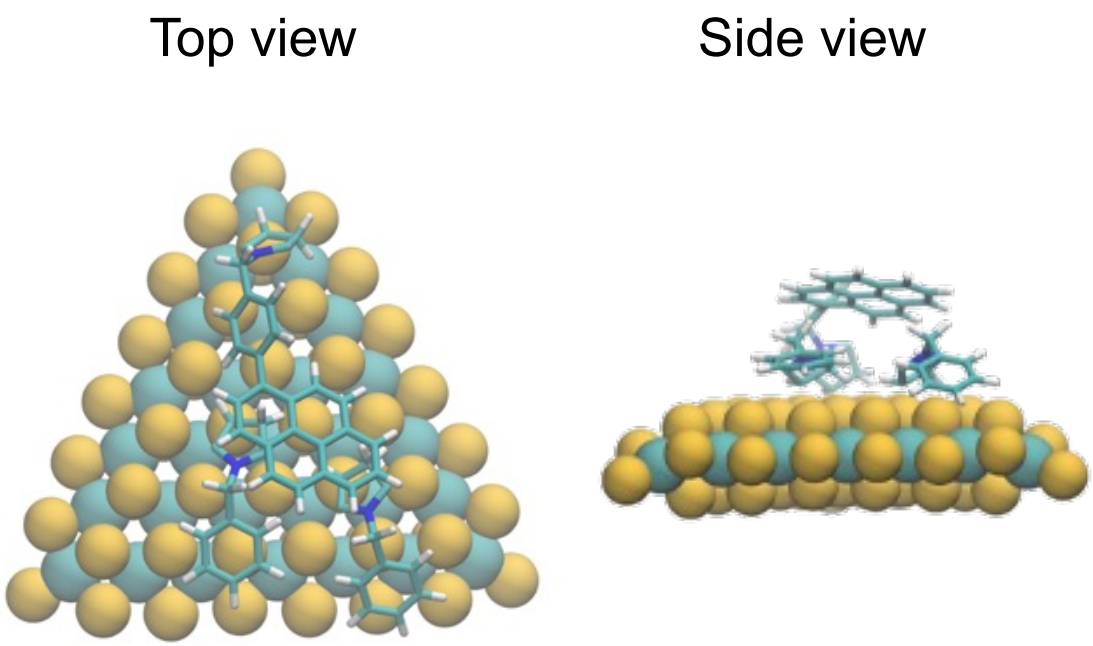

Fig. S17 Structure of Py-Bn-MoS_2 model. One *N*-*p*-pyrenylbenzylsuccinimide unit and two *N*-benzylsuccinimide units are covalently attached to the S atoms marked with C and A, respectively, in the $Mo_{28}S_{63}$ nanosheet (Fig. S10b). Two *N*-benzylsuccinimide units at the other S atoms marked with C are omitted for simplicity due to the absence of the interaction with the Py unit.

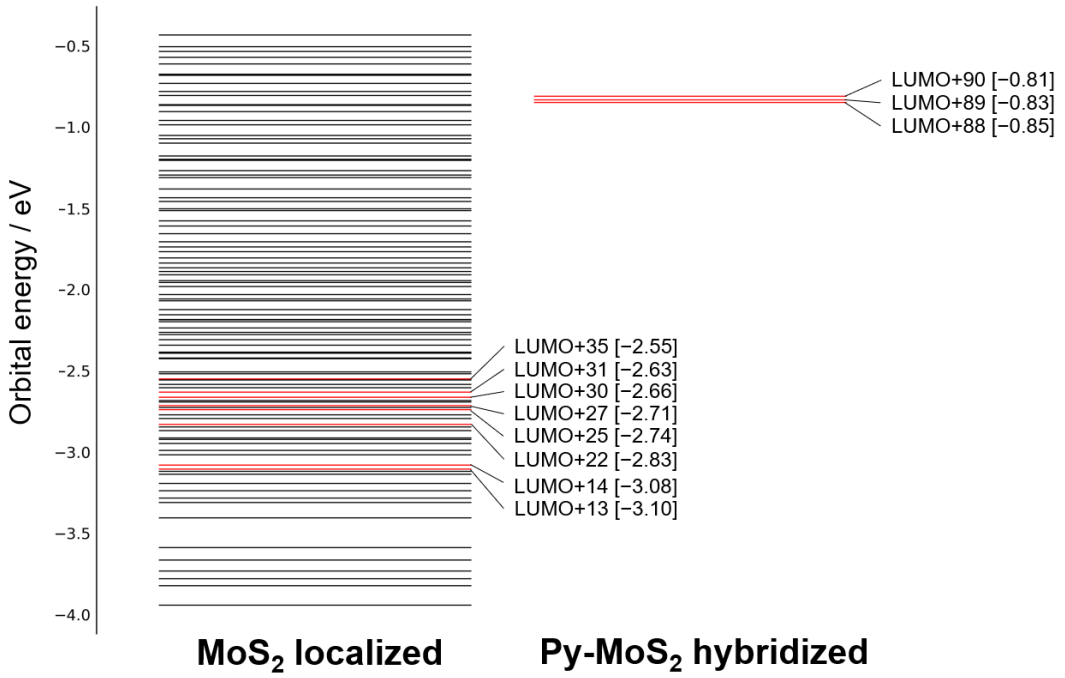

Fig. S18 Energy distribution of vacant orbitals of Py-Bn-MoS_2 model from LUMO to LUMO+100. MoS_2 localized orbitals and pyrene-MoS_2 hybridized orbitals are shown separately for clarity. The red lines represent vacant orbitals with large contributions to the CT emission. The values in square brackets indicate the orbital energies.

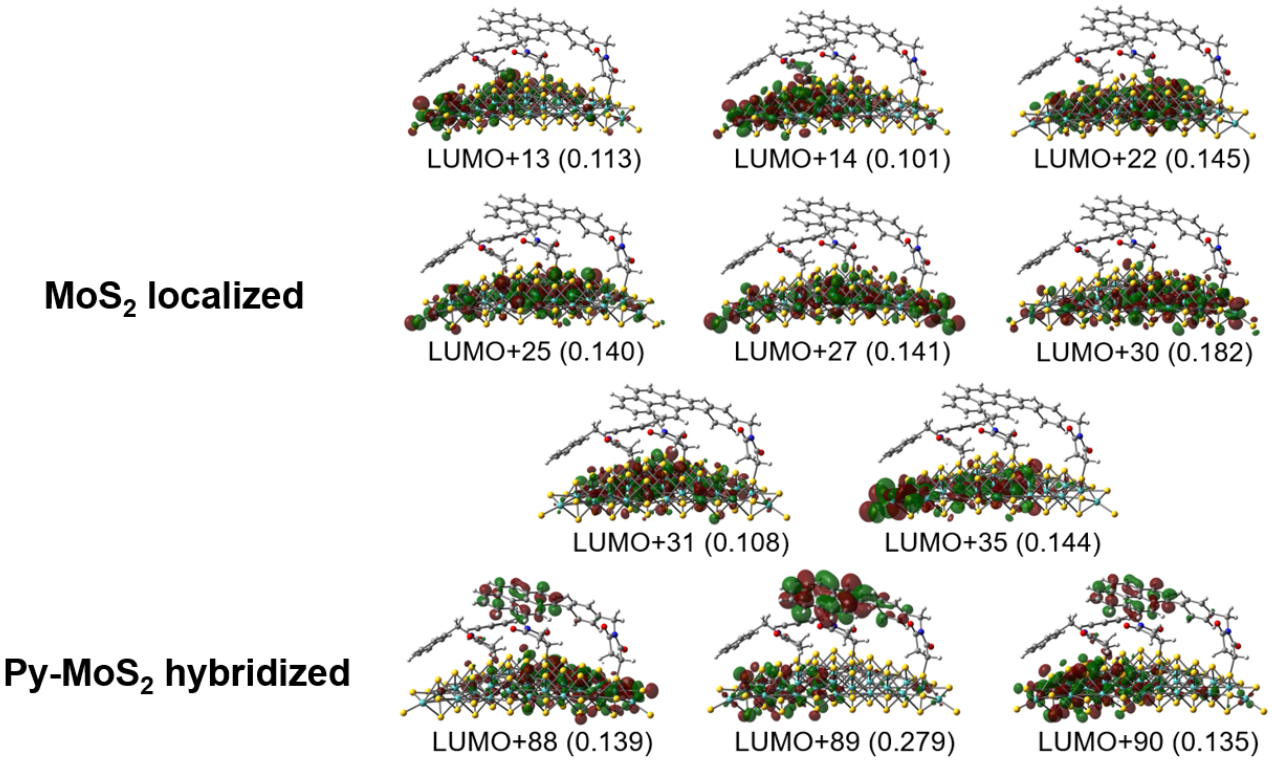

Fig. S19 Vacant orbitals of Py-Bn-MoS_2 model with large contribution to the CT emission. The numbers in parenthesis represent the absolute values of coefficients of transition from the HOMO.

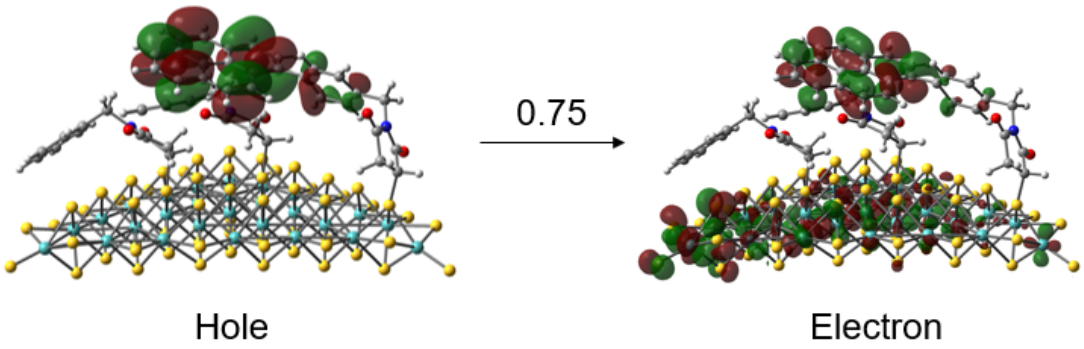

Fig. S20 The NTOs with the largest contribution (occupations = 0.75) to the CT emission of Py-Bn-MoS_2 model. The occupations of the other NTOs were less than 0.03.

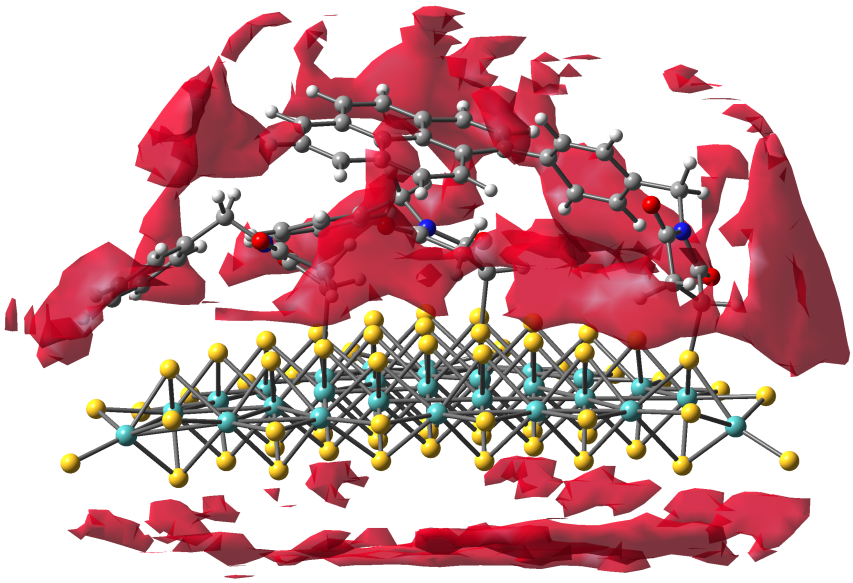

Fig. S21 Spatial distribution functions of oxygen atom of DMSO solvent in the emission states of Py-Bn-MoS_2 model calculated with the 3D-RISM method. Isovalue was set to be 3.4. Py is strongly solvated by the oxygen atom of DMSO because Py is positively charged by the charge-transfer character of the emission state.

9. References

[S1] J. J. Snellenburg, S. P. Laptenok, R. Seger, K. M. Mullen, K. M. and I. H. M. van. Stokkum, *J. Stat. Softw.*, 2012, **49**, 1.

[S2] T. Li and G. Galli, *J. Phys. Chem. C*, 2007, **111**, 16192.

[S3] D. Cao, T. Shen, P. Liang, X. Chen and H. Shu, *J. Phys. Chem. C*, 2015, **119**, 4294.

[S4] H. Sun, J. Autschbach, *J. Chem. Theory Comput.* 2014, **10**, 1035.

[S5] T. M. McCormick, C. R. Bridges, E. I. Carrera, P. M. DiCarmine, G. L. Gibson, J. Hollinger, L. M. Kozycz and D. S. Seferos, *Macromolecules*, 2013, **46**, 3879.

[S6] A. Kovalenko and F. Hirata, *J. Chem. Phys.*, 1999, **110**, 10095.

[S7] M. Caricato, B. Mennucci, J. Tomasi, F. Ingrosso, R. Cammi, S. Corni and G. Scalmani, *J. Chem. Phys.*, 2006, **124**, 124520.

[S8] B. H. Besler, B. H.; K. M. Merz Jr. and P. A. Kollman, *J. Comput. Chem.*, 1990, **11**, 431.

[S9] J. Liu J. Zeng, C. Zhu, J. Miao, Y. Huang and H. Heinz, *Chem. Sci.*, 2020, **11**, 8708.

[S10] W. L. Jorgensen, D. S. Maxwell and J. Tirado-Rives, *J. Am. Chem. Soc.*, 1996, **118**, 11225.

[S11] M. J. Frisch, G. W. Trucks, H. B. Schlegel, G. E. Scuseria, M. A. Robb, J. R. Cheeseman, G. Scalmani, V. Barone, G. A. Petersson, H. Nakatsuji, X. Li, M. Caricato, A. V. Marenich, J. Bloino, B. G. Janesko, R. Gomperts, B. Mennucci, H. P. Hratchian, J. V. Ortiz, A. F. Izmaylov, J. L. Sonnenberg, D. Williams-Young, F. Ding, F. Lipparini, F. Egidi, J. Goings, B. Peng, A. Petrone, T. Henderson, D. Ranasinghe, V. G. Zakrzewski, J. Gao, N. Rega, G. Zheng, W. Liang, M. Hada, M. Ehara, K. Toyota, R. Fukuda, J. Hasegawa, M. Ishida, T. Nakajima, Y. Honda, O. Kitao, H. Nakai, T. Vreven, K. Throssell, J. A. Montgomery, Jr., J. E. Peralta, F. Ogliaro, M. J. Bearpark, J. J. Heyd, E. N. Brothers, K. N. Kudin, V. N. Staroverov, T. A. Keith, R. Kobayashi, J. Normand, K. Raghavachari, A. P. Rendell, J. C. Burant, S. S. Iyengar, J. Tomasi, M. Cossi, J. M. Millam, M. Klene, C. Adamo, R. Cammi, J. W. Ochterski, R. L. Martin, K. Morokuma, O. Farkas, J. B. Foresman and D. J. Fox, Gaussian 16, Revision A.03, Gaussian, Inc., Wallingford CT, 2016.

[S12] N. Yoshida and F. Hirata, *J. Comput. Chem.*, 2006, **27**, 453.

[S13] N. Yoshida, Y. Kiyota and F. Hirata, *J. Mol. Liq.*, 2011, **159**, 83.

[S14] E. Schweizer, A. Hoffmann-Roeder, J. A. Olsen, P. Seiler, U. Obst-Sander, B. Wagner, M. Kansy, D. W. Banner and F. Diederich, *Org. Biomol. Chem.*, 2006, **4**, 2364.

[S15] T. Umeyama, J. Baek, Y. Sato, K. Suenaga, F. Abou-Chahine, N. V. Tkachenko, H. Lemmetyinen and H. Imahori, *Nat. Commun.*, 2015, **6**, 7732.